

# Amphiphilic Molecules Exhibiting Zwitterionic Excited-State Intramolecular Proton Transfer and Near-Infrared Emission for the Detection of Amyloid $\beta$ Aggregates in Alzheimer's Disease\*\*

Zhengxin Yu,<sup>[a]</sup> Yusuff Moshood,<sup>[a]</sup> Marcin K. Wozniak,<sup>[b]</sup> Shrey Patel,<sup>[a]</sup> Karna Terpstra,<sup>[a]</sup> Daniel A. Llano,<sup>[c]</sup> Lawrence W. Dobrucki,<sup>[b]</sup> and Liviu M. Mirica<sup>\*[a, d]</sup>

Chromophores with zwitterionic excited-state intramolecular proton transfer (ESIPT) have been shown to have larger Stokes shifts and red-shifted emission wavelengths compared to the conventional  $\pi$ -delocalized ESIPT molecules. However, there is still a dearth of design strategies to expand the current library of zwitterionic ESIPT compounds. Herein, a novel zwitterionic excited-state intramolecular proton transfer system is reported, enabled by addition of 1,4,7-triazacyclononane (TACN) fragments on a dicyanomethylene-4H-pyran (DCM) scaffold. The solvent-dependent steady-state photophysical studies, pKa measurements, and computational analysis strongly support that the ESIPT process is more efficient with two TACN groups

attached to the DCM scaffold and not affected by polar protic solvents. Impressively, compound DCM-OH-2-DT exhibits a near-infrared (NIR) emission at 740 nm along with an uncommonly large Stokes shift. Moreover, DCM-OH-2-DT shows high affinity towards soluble amyloid  $\beta$  ( $A\beta$ ) oligomers in vitro and in 5xFAD mouse brain sections, and we have successfully applied DCM-OH-2-DT for the in vivo imaging of  $A\beta$  aggregates and demonstrated its potential use as an early diagnostic agent for AD. Overall, this study can provide a general molecular design strategy for developing new zwitterionic ESIPT compounds with NIR emission in vivo imaging applications.

## Introduction

Excited-State Intramolecular Proton Transfer (ESIPT) is a four-level photochemical process that generates an intramolecular tautomer. Since the first report in the 1950s,<sup>[1]</sup> it has shown significant impact in various areas, including physiology, pharmacology, environmental science, chemical and bioimaging probes, as well as organic electronics and organic lasers.<sup>[2]</sup> Conventionally, the ESIPT molecules, such as derivatives of 2-(2'-hydroxyphenyl)benzothiazole (HBT), 2-(2'-hydroxyphenyl)benzimidazole (HBI), utilize  $\pi$ -delocalization for proton transfer and exhibit an enol (E) to keto (K) photo-tautomerization process.<sup>[3]</sup> Emerging evidence shows that a charge redistribution could lead to a zwitterionic form (PT) in the excited state.<sup>[4]</sup> For example, the zwitterionic (PT) excited states have been shown to exist for the following scaffolds: pyrrole-containing oligoarenes that involve a strap strategy with N–H...N-based hydrogen bonding;<sup>[4a]</sup> a 3-thioflavone platform with an excited-state intramolecular thiol S–H...O proton transfer;<sup>[4b]</sup> and a traditional HBT platform but with two fluorene groups attached.<sup>[4c]</sup> Interestingly, extremely large Stokes shifts and significant red-shifted emission wavelengths were observed from the zwitterionic ESIPT molecules, even when compared to the conventional  $\pi$ -delocalized ESIPT molecules.<sup>[4b,c]</sup> These large Stokes shifts and redshifts of the emission wavelengths are especially attractive features for chemical, biosensing, and imaging applications. However, the dearth of strategies to develop such unique zwitterionic ESIPT molecules limit further exploration of their potential applications.

[a] Z. Yu, Y. Moshood, S. Patel, K. Terpstra, L. M. Mirica  
Department of Chemistry  
Beckman Institute for Advanced Science and Technology  
The Neuroscience Program, Carle Illinois College of Medicine  
University of Illinois at Urbana-Champaign  
600 S. Mathews Avenue, Urbana, Illinois 61801 (USA)  
E-mail: mirica@illinois.edu

[b] M. K. Wozniak, L. W. Dobrucki  
Beckman Institute for Advanced Science and Technology  
Department of Bioengineering  
University of Illinois at Urbana-Champaign  
Urbana IL 61801 (USA)

[c] D. A. Llano  
Beckman Institute for Advanced Science and Technology  
Department of Molecular and Integrative Physiology  
University of Illinois at Urbana-Champaign  
Urbana IL 61801 (USA)

[d] L. M. Mirica  
Hope Center for Neurological Disorders  
Washington University School of Medicine  
St. Louis, MO 63110 (USA)

[\*\*] A previous version of this manuscript has been deposited on a preprint server (<https://doi.org/10.26434/chemrxiv-2022-3gxlh>).

Supporting information for this article is available on the WWW under <https://doi.org/10.1002/chem.202302408>

© 2023 The Authors. Chemistry - A European Journal published by Wiley-VCH GmbH. This is an open access article under the terms of the Creative Commons Attribution Non-Commercial NoDerivs License, which permits use and distribution in any medium, provided the original work is properly cited, the use is non-commercial and no modifications or adaptations are made.

Protein misfolding and aggregation are highly associated with the progression of Alzheimer's Disease (AD), which is the most prevalent neurodegenerative disease.<sup>[5]</sup> One hallmark of AD, the amyloid plaques, are formed from the aggregation of the beta-amyloid (A $\beta$ ) peptide.<sup>[6]</sup> During the aggregation process, a variety of intermediate A $\beta$  species exist, such as smaller soluble A $\beta$  oligomers and protofibrils. Soluble A $\beta$  oligomers are relevant in both the physiology and pathology of AD and dominate the early stages of the disorder, making them a potential biomarker for early diagnosis.<sup>[7]</sup> However, due to the lack of an atomic structure for these oligomeric species, there is still great challenge to develop imaging agents targeting the soluble A $\beta$  oligomers.<sup>[8]</sup> Great efforts had been made in the past few decades to distinguish the different aggregation stages of the amyloid proteins.<sup>[9]</sup> For example, several A $\beta$  oligomer-specific fluorescent probes have been developed,<sup>[10]</sup> based either on restriction of the molecular rotation<sup>[11]</sup> or probes exhibiting FRET behavior.<sup>[12]</sup> However, some of these probes have limited *in vivo* applications. Moreover, a ruthenium polypyridyl complex has also been designed and developed by Marti et al. for A $\beta$  oligomer detection via photoluminescence anisotropy.<sup>[13]</sup> Recently, our group demonstrated that incorporating amphiphilic properties into small molecule design increases their selectivity towards A $\beta$  oligomers and hence will be beneficial for A $\beta$  oligomer detection.<sup>[14]</sup> Even though different strategies have been applied, *in vivo* imaging agents targeting A $\beta$  oligomers are still highly needed, in order to expand the current toolbox of early diagnostic agents for AD.<sup>[15]</sup>

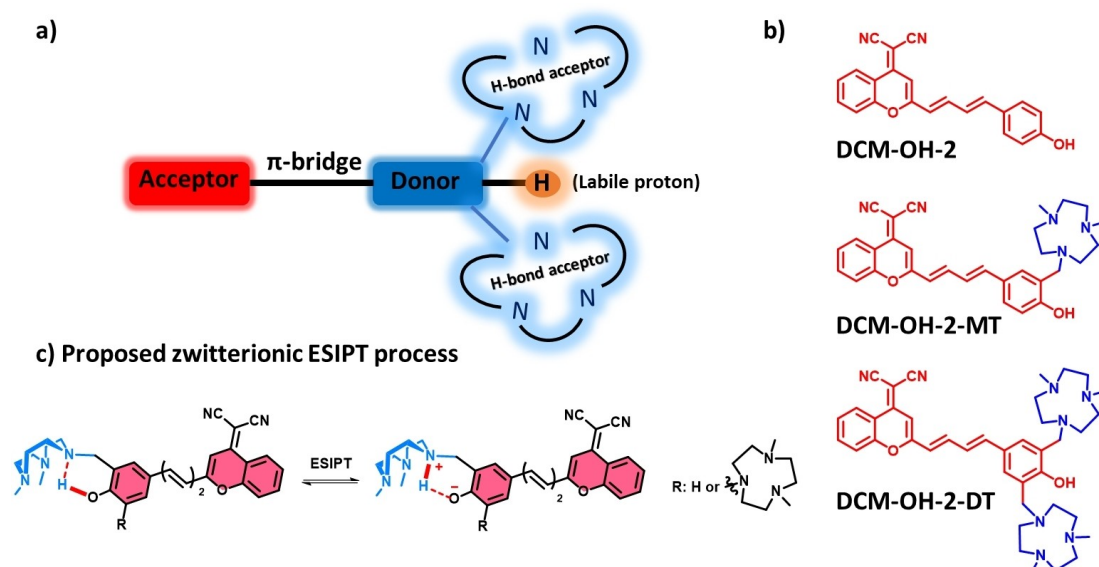
Herein, we report a novel zwitterionic excited-state intramolecular proton transfer system enabled by appending one or two 1,4,7-triazacyclononane (TACN) molecular fragments on a dicyanomethylene-4H-pyran (DCM) scaffold. From the solvent-dependent steady-state photophysical studies, density functional theory (DFT) calculations, and time-dependent DFT (TD-DFT) studies, we demonstrate that the zwitterionic ESIPT of DCM-OH-2-DT is more efficient than that of DCM-OH-2-MT. Moreover, the imaging applications of the developed compounds are further explored in a transgenic AD mouse model. With the hydrophilic TACN group(s) attached, the developed amphiphilic compounds were shown to be able to interact with the A $\beta$  oligomers *in vitro*, as shown on the brain sections of transgenic AD mice. Excitingly, we also demonstrate that compound DCM-OH-2-DT can readily penetrate the blood-brain barrier (BBB) and shows significantly higher near-infrared (NIR) fluorescence intensity in the 5xFAD mice vs. wild-type (WT) controls. Lastly, these amphiphilic compounds can bind Cu(II) ions strongly, indicating their potential future use in <sup>64</sup>Cu positron emission tomography (PET) imaging of A $\beta$  species in AD.

## Results and Discussion

### Zwitterionic excited-state intramolecular proton transfer enabled by azamacrocycles

Yamaguchi and coworkers reported that alkyl-amino groups embedded in an alkyl strap on the pyrrole-containing oligoarenes scaffold facilitate the ESIPT process to generate zwitterionic ESIPT molecules.<sup>[4a,16]</sup> The hydrogen bonding interactions between the amino groups and the pyrrole N–H proton, as well as the boryl groups serving as electron acceptors in the  $\pi$ -conjugated system are the two critical components for their design. However, imaging applications for these zwitterionic ESIPT molecules have not been explored due to less facile in chemical modifications. To explore the imaging applications for the unique zwitterionic ESIPT photochemical process, we postulate that a labile hydrogen bond donor (e.g., a phenol O–H proton), a D- $\pi$ -A structure as the conjugated system to stabilize the charge separated excited state, and an appropriate hydrogen bond acceptor are necessary to generate zwitterionic ESIPT molecules (Scheme 1a). Therefore, our molecular design focus on the following components: a typical D- $\pi$ -A structure is constructed by utilizing dicyanomethylene as the electron acceptor and phenol as the electron donor, which are linked via two C=C double bonds, while a 2,4-dimethyl-1,4,7-triazacyclononane (Me<sub>2</sub>HTACN) fragment is chosen as a hydrogen bond acceptor and is installed ortho to the phenol group. Moreover, none, one, or two Me<sub>2</sub>TACN groups are installed to compare and validate the ESIPT process. With this molecular design, three compounds were designed and synthesized: DCM-OH-2, DCM-OH-2-MT, and DCM-OH-2-DT (Scheme 1b). The synthetic details and spectroscopy characterizations (<sup>1</sup>H, <sup>13</sup>C NMR, HPLC and HR-ESI) can be found in the Supporting Information.<sup>[17]</sup>

With the three compounds in hand, we first compared their photophysical properties. The absorbance of the three compounds in EtOH shows no significant difference, with maximum absorption at around 470 nm (Figure S1a). However, their emission properties differ greatly. DCM-OH-2 emits at 625 nm, DCM-OH-2-MT exhibits two peaks at 615 nm and 740 nm, and DCM-OH-2-DT has a single peak at 740 nm (Figure 1a). Normally, two emission peaks from a locally excited (LE) state and an ESIPT state are observed for the compounds that can go through the ESIPT process.<sup>[18]</sup> We believe the newly developed compounds with TACN groups attached would undergo the ESIPT process to generate new zwitterionic species, as proposed in Scheme 1. To further elucidate the differences in emission behaviors, several experiments were performed. Firstly, the fluorescence excitation spectra for DCM-OH-2-MT are similar to its absorption spectrum, regardless of the 615 nm or 740 nm emission peak probed (Figure S1b), indicating that the two emission peaks originate from the same ground state. Secondly, the emission spectra of the compounds in several solvents with different polarities were recorded (Figure 1b). The maximum emission wavelength for DCM-OH-2 increases as the polarity of the solvent increases, suggesting that the compound would go through an intramolecular charge transfer (ICT) process at the excited state.<sup>[19]</sup> While DCM-OH-2-MT emits at a longer wave-



**Scheme 1.** a) Molecular design of the zwitterionic ES IPT molecule enabled by azamacrocycles. b) Chemical structure of DCM-OH-2, DCM-OH-2-MT and DCM-OH-2-DT. c) Proposed zwitterionic ES IPT process.

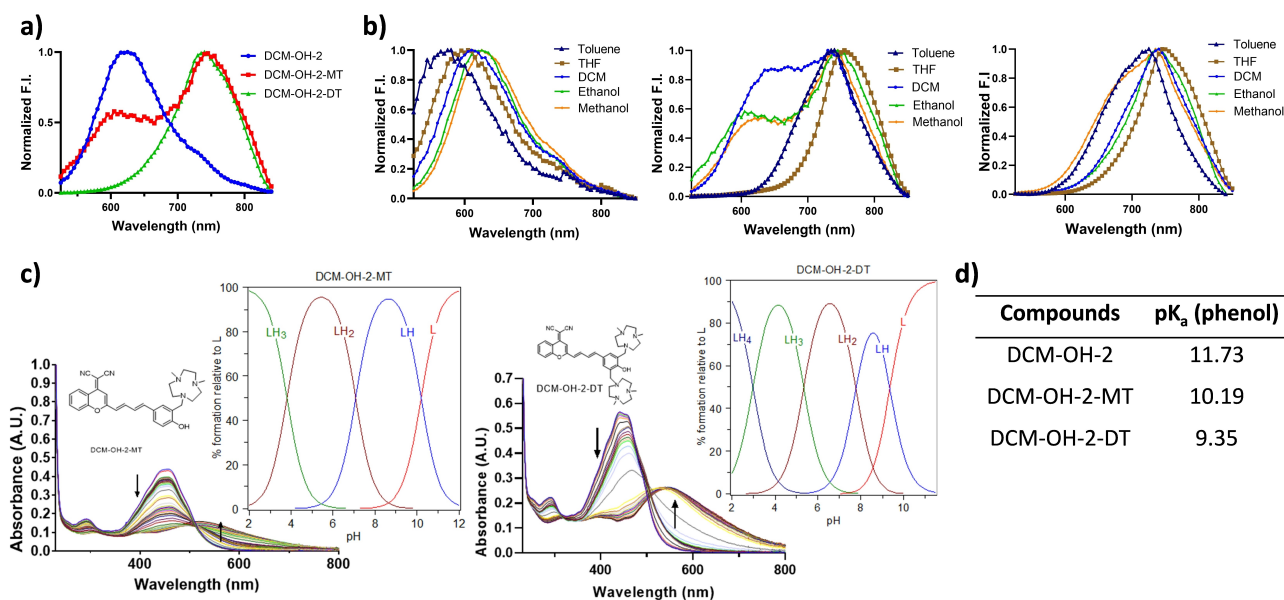


**Figure 1.** a) Emission spectra of the compounds (10  $\mu$ M) in EtOH. b) Emission spectra of the compounds (10  $\mu$ M) in different solvents: DCM-OH-2 (left), DCM-OH-2-MT (middle), and DCM-OH-2-DT (right). c) Variable pH (pH 3–11) UV-vis spectra of DCM-OH-2 s compounds ([DCM-OH-2-MT] = 20  $\mu$ M, [DCM-OH-2-DT] = 30  $\mu$ M 25  $^{\circ}$ C, I = 0.1 M NaCl) and the corresponding species distribution plots. d) Calculated pK<sub>a</sub> values of the phenol groups for DCM-OH-2, DCM-OH-2-MT, and DCM-OH-2-DT, obtained from the spectrophotometric titrations.

length in solvents with lower polarity (e.g., toluene and THF) and the shorter wavelength emission appears as a shoulder peak in polar protic solvents (e.g., MeOH and EtOH), the emission of DCM-OH-2-DT was unaffected by solvent polarity or protic/aprotic properties, suggesting that the ES IPT is more efficient for DCM-OH-2-DT compared to DCM-OH-2-MT.

The macrocyclic TACN groups are in close proximity to the phenol group and can act as proton 'chelators'/hydrogen bond acceptors. As the formation of an intramolecular hydrogen bond is a prerequisite and can greatly affect the ES IPT process,

we therefore investigated the effects of TACN groups on the hydrogen bond formation. We measured the acidity constants (i.e., pK<sub>a</sub> values) of the developed DCM compounds using spectrophotometric titrations (Table S1 and Figures S2 and S3). The largest pK<sub>a</sub> value was assigned to the phenol O–H due to significant spectral changes. With one TACN group, the pK<sub>a</sub> value decreased from 11.73 to 10.19 for DCM-OH-2-MT and further to 9.35 for DCM-OH-2-DT. This suggests an increased acidity of the phenol proton and stronger intramolecular hydrogen bonding interactions in DCM-OH-2-DT. It is also worth

noting that the hydrogen bonding interactions between phenol and the alkyl amino group at the ortho position was observed in the solid state for some metal chelators, such as carbohydrate-containing compounds.<sup>[20]</sup> Collectively, these data suggest that with two TACN macrocycles attached, the ESIPT is more efficient and not affected by the polarity of solvent. This property is necessary and beneficial for their potential applications under physiologically relevant aqueous conditions.

Next, a series of density functional theory (DFT) and time-dependent DFT (TD-DFT) studies were performed to understand the electronic properties of the developed compounds in their ground state ( $S_0$ ) and the lowest-energy excited singlet state ( $S_1$ ). The geometry optimizations were conducted using the CAM-B3LYP hybrid density functional along with the 6-31G(d,p) basis set, and the solvation effect of water was taken into consideration via the solvation model density (SMD) model. The calculated absorption and emission profiles of all compounds were summarized in energy-level diagrams (Figures 2 and S4c). The excitation wavelengths of DCM-OH-2, DCM-OH-2-MT, and DCM-OH-2-DT are calculated to be 416 nm, 422 nm, and 426 nm, respectively, with a slight blue shift compared to the experimental absorption maxima in water (Figure S4a). DCM-OH-2 emits only from the locally excited (LE) state at 573 nm, while the experimental emission maximum in water is 670 nm (Figure S4b), likely due to significant intramolecular charge-transfer characteristics. For DCM-OH-2-DT, the calculated PT- $S_1$  state is 372 mV (8.58 kcal/mol) below the E- $S_1$  state, indicating a thermodynamically favorable ESIPT process. Furthermore, the calculated fluorescence from the E- $S_1$  and PT- $S_1$  states occurs at 638 nm and 707 nm, matching reasonably well with the

experimental values (Figure S4b). The calculations for DCM-OH-2-MT indicate that the fluorescence from the E- $S_1$  and PT- $S_1$  states occurs at 631 nm and 698 nm, respectively, with the PT- $S_1$  state still favored over the E- $S_1$  state. However, the experimental data showed an inverse distribution with a maximum peak located at 640 nm and a shoulder peak at 740 nm in a ~2:1 ratio. Therefore, more detailed calculations involving hydrogen bonding interactions with the solvent molecule might be needed for DCM-OH-2-MT to explain the experimental data.

To further elucidate the role of the macrocycles, we compared the hydrogen bonding interactions in DCM-OH-2-MT and DCM-OH-2-DT (Table S5). The calculated N...H-O distances are 1.740 Å and 1.739 Å for DCM-OH-2-MT and DCM-OH-2-DT at the E- $S_0$  states, while they become significantly shorter at the corresponding E- $S_1$  states (1.590 Å for DCM-OH-2-MT and 1.576 Å for DCM-OH-2-DT, respectively, Figure 2c). The shorter N...H-O distances at the excited states indicate the enhanced hydrogen bonding interactions, which are more significant for DCM-OH-2-DT, are likely facilitating ESIPT. Moreover, the calculated O...H-N distance at the PT- $S_0$  state for DCM-OH-2-DT (1.908 Å) is also shorter than that for DCM-OH-2-MT (1.957 Å, Figure 2d), suggesting a reverse proton transfer process might be more accessible for DCM-OH-2-DT. Taken together, we believe the highly efficient ESIPT for DCM-OH-2-DT is likely promoted by the enhanced intramolecular hydrogen bonding interactions. Lastly, DCM-OH-2-DT shows a smaller dipole moment at the E- $S_0$  state than DCM-OH-2-MT (20.8 D vs. 20.9 D), but larger dipole moments (28.6 D and 40.1 D) at the E- $S_1$  and PT- $S_1$  excited states than those of DCM-OH-2-MT (28.4 D and

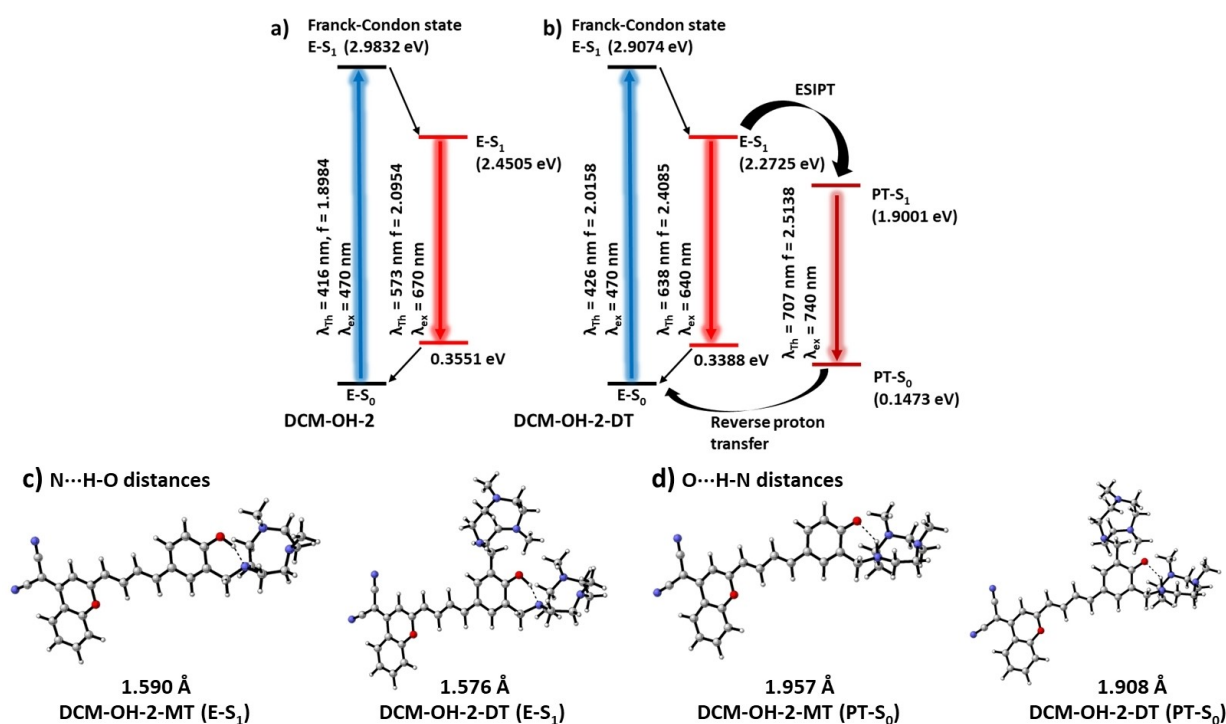


**Figure 2.** Calculated energy-level diagrams along with the oscillator strength ( $f$ ) for a) the E forms of DCM-OH-2 and b) the E and PT forms of DCM-OH-2-DT at the CAM-B3LYP/6-31G(d,p)/SMD level. c) and d) Calculated hydrogen bonding distances at E- $S_1$  and PT- $S_0$  states for DCM-OH-2-MT and DCM-OH-2-DT.  $\lambda_{th}$  and  $\lambda_{ex}$  represent the theoretical and experimentally measured wavelengths, respectively.

39.9 D at the E-S<sub>1</sub> and PT-S<sub>1</sub> state, respectively, Table S5 and S6). The large dipole moments at the excited states indicate the zwitterionic character and potential for greater stabilization in polar solvents. Overall, this computational analysis reveals the energetic and structural differences between the compounds and strongly supports the efficient ESIPT process when two azamacrocycles are attached to the fluorophore.

### In vitro interactions between the amphiphilic compounds and amyloid $\beta$ aggregates

Our molecular design resembles some extended rotor-based fluorophores (RBFs), in which the electron donor and electron acceptor are linked via conjugated C=C double instead of C-C single bond. It was demonstrated that extended RBFs are capable of detecting amyloid-oligomeric species formed during protein aggregation.<sup>[21]</sup> While some DCM derivatives were applied for A $\beta$  aggregates detection in a AD mouse model, the majority of them have only been reported to detect A $\beta$  fibrils.<sup>[10e,22]</sup> With the hydrophilic TACN groups attached, the resulting amphiphilic DCM compounds might have enhanced affinity/selectivity towards soluble A $\beta$  oligomers.<sup>[14]</sup> Therefore, we are encouraged to investigate the emission and binding

properties of the developed DCM compounds upon A $\beta$  binding, and their potential usage as in vivo diagnostic agents.

Two types of A $\beta$  aggregates, insoluble A $\beta$  fibrils and soluble A $\beta$  oligomers, were prepared to investigate the interactions between the compounds and A $\beta$  aggregates.<sup>[23]</sup> Compound DCM-OH-2 exhibits a significant fluorescence turn-on effect with a shift in maximum emission wavelength from 680 nm to 620 nm when incubated with A $\beta$  aggregates in PBS (Figure 3a), indicating the binding mechanism of RBFs and the increased hydrophobicity at the binding pocket for DCM-OH-2. The dramatic hypochromic shift results in the emission wavelength being located outside the NIR window (>650 nm), thereby limiting the in vivo imaging applications for DCM-OH-2.<sup>[24]</sup> In contrast, DCM-OH-2-DT shows a single NIR emission peak at about 730 nm in the presence of A $\beta$  aggregates (Figure 3a). DCM-OH-2-MT exhibits two emission peaks at 620 nm and 730 nm, which could be attributed to LE and ESIPT emission, respectively (Figure 3a). These emission differences further confirm that with two TACN groups attached, the ESIPT process is not affected by the polarity of the surrounding environment (e.g., the binding pockets of the A $\beta$  aggregates). Moreover, we also systematically investigated the effects of number of double bonds on A $\beta$  targeting abilities and synthesized and characterized DCM-OH-1 and DCM-OH-3 compounds, which have one and three double bonds, respectively (Schemes S2 and S3).

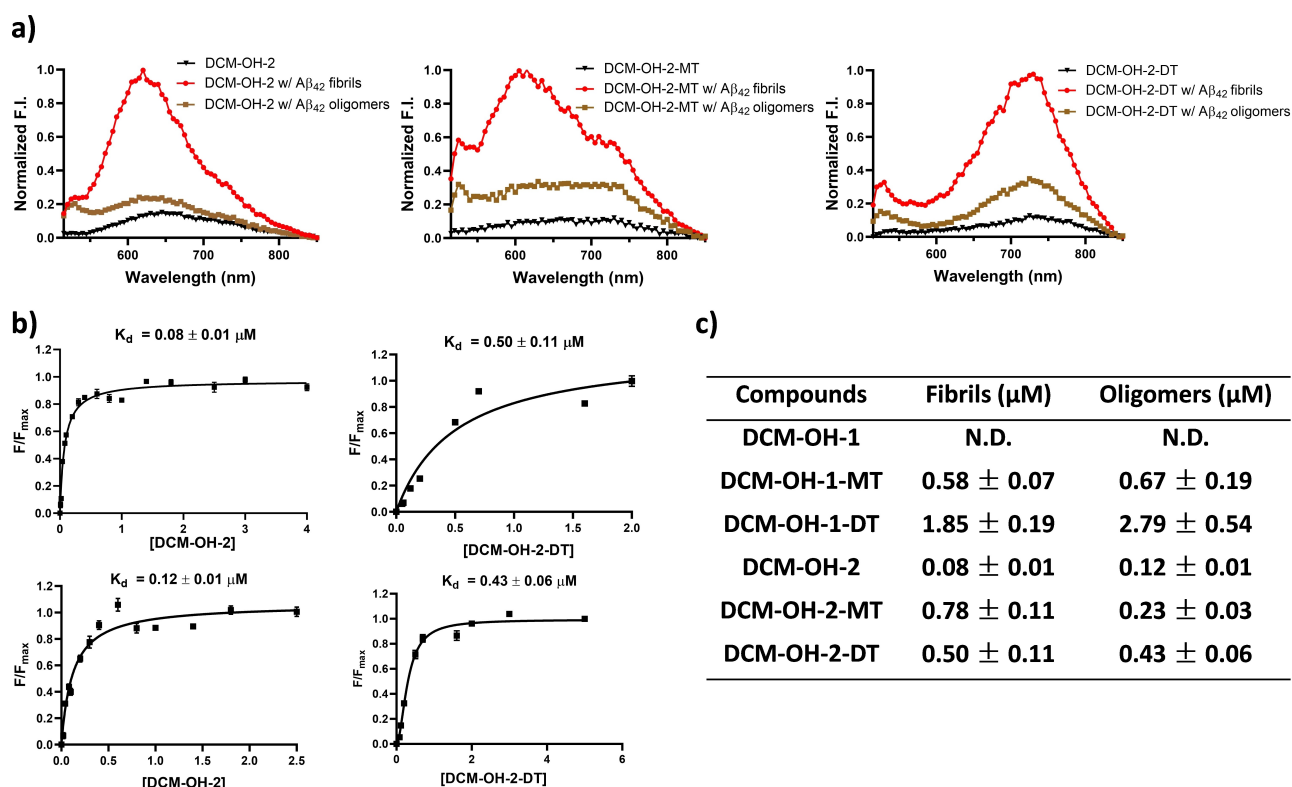


**Figure 3.** a) Fluorescence turn-on effects with A $\beta$ <sub>42</sub> oligomers and fibrils. Left: DCM-OH-2, middle: DCM-OH-2-MT, and right: DCM-OH-2-DT. Black: compound only; Brown: compound + A $\beta$ <sub>42</sub> oligomers; Red: compound + A $\beta$ <sub>42</sub> fibrils; [compound] = 5  $\mu$ M; [A $\beta$ <sub>42</sub> oligomers] = 25  $\mu$ M; [A $\beta$ <sub>42</sub> fibrils] = 25  $\mu$ M. Fluorescence intensity was collected from 515 nm to 850 nm upon excitation at 470 nm. b) Binding constant measurements of DCM-OH-2 (left), DCM-OH-2-DT (right) with A $\beta$ <sub>42</sub> fibrils (top), and A $\beta$ <sub>42</sub> oligomers (bottom). The K<sub>d</sub> curves were fitted in GraphPad Prism with one site-specific binding model. Equation:  $Y = B_{max} * X / (K_d + X)$ . c) Summarized K<sub>d</sub> values for the DCM-based compounds (see other fitting curves in Supporting Information). N.D.: not determined. All measurements were conducted in PBS (10 mM, pH 7.4).

Interestingly, DCM-OH-1-MT and DCM-OH-1-DT showed fluorescence enhancement with their maximum emission located at the edge of the NIR window (~650 nm), while DCM-OH-3-MT and DCM-OH-3-DT did not exhibit fluorescence turn-on effects in the NIR region (Figures S4 and S5).

Fluorescence saturation assays were conducted to determine the binding affinities of the developed compounds (Figures 3bc, S6, and S7). Compounds with two double bonds (DCM-OH-2 s) had higher affinities than compounds with one double bond (DCM-OH-1 s), with DCM-OH-2 exhibiting the highest affinities towards both A $\beta$  fibrils (~80 nM) and A $\beta$  oligomers (~120 nM). For DCM-OH-2-MT, the affinity towards A $\beta$  oligomers (~230 nM) is about three times higher than its affinity towards A $\beta$  fibrils (~780 nM). We observed that DCM-OH-2-DT though still favors A $\beta$  oligomers over A $\beta$  fibrils, while showing a slightly lower affinity towards A $\beta$  oligomers (~430 nM) compared to DCM-OH-2-MT, which may be due to the increased steric hindrance. Moreover, both DCM-OH-2-MT and DCM-OH-2-DT demonstrate remarkable selectivity towards A $\beta_{42}$  aggregates when compared to various analytes, including a diverse range of amino acids, metal ions, and serum albumins (Figure S8a and S8b). The assessment of photostability for DCM-OH-2-MT and DCM-OH-2-DT, both in the presence and absence of A $\beta_{42}$  aggregates, further reinforces their suitability for long-term imaging applications (in Figure S8c and S8d). Molecular docking studies were performed with DCM-OH-2s to understand their interactions with A $\beta$  fibrils and A $\beta$  oligomers (Figure S9). DCM-OH-2 binds to the  $\beta$ -sheet structure of A $\beta$  fibrils (PDB: 5OQV), but also exhibits hydrogen bonding interactions with Lys 28. Interestingly, DCM-OH-2-MT interacts with the hydrophobic C-terminus of one A $\beta$  peptide and the hydrophilic N-terminus of another A $\beta$  peptide. DCM-OH-2-DT exhibits multiple interactions with A $\beta$  fibrils, including hydrogen bonding interactions with the side chain of Asn 27 and the backbone of Val 18, as well as the  $\pi$ -cation interactions with Phe 19. When the molecules are docked onto the oligomeric A $\beta$  structure (PDB: 6RHY), all molecules interact with the  $\beta$ -sheet structure and exhibit hydrophilic interactions. Specifically, hydrogen bonding interactions with His 6, Asp 7 and Gly 25 are observed for DCM-OH-2, interactions with His 6 are observed

for DCM-OH-2-MT, and interactions with Asp 7, Val 24 and Ala 42 are observed for DCM-OH-2-DT, respectively. The docking scores and Glide e-model energies (kcal/mol) for all compounds are summarized in Table S2. Importantly, DCM-OH-2-DT (-4.45 and -60.0 kcal/mol) shows smaller docking score and lower Glide e-model energy comparing that to DCM-OH-2 (-2.99 and -33.7 kcal/mol) and DCM-OH-2-MT (-2.93 and -40.2 kcal/mol) when docked to A $\beta$  oligomer structure, indicating the formation of a more stable compound-A $\beta$  adduct. Therefore, we strongly believe the hydrophilic TACN groups contribute to the enhanced interactions with A $\beta$  oligomers. Taken all together, the low  $K_d$  value of DCM-OH-2-DT and long wavelength emission support the binding and targeting abilities towards A $\beta$  oligomers, which is essential for further in vivo studies.

### Detection of low-viscosity oligomers in vitro and in 5xFAD mouse brain sections

Since the DCM-OH-2-based compounds have the desired emission and A $\beta$  binding properties, the following studies mainly focus on these compounds. It was demonstrated that RBFs with high viscosity sensitivity only emit strong fluorescence in a high viscous environment such as insoluble aggregates, while RBFs with low viscosity sensitivity can maintain strong fluorescence in misfolded oligomers with low viscosity.<sup>[21]</sup> Therefore, we obtained fluorescence intensities of these compounds in a series of mixtures and extracted viscosity sensitivity  $x$  values using the Förster-Hoffmann equation  $\log(I) = x \log(\eta) + C$ .<sup>[25]</sup> The larger the  $x$  value is, the higher viscosity sensitivity a compound has. The DCM-OH-2-based compounds exhibit much lower  $x$  values compare to Thioflavin T (ThT, Figures 4a and 4b), a well-known RBF for amyloid fibrillar structures.<sup>[26]</sup> Compound DCM-OH-2-DT exhibits the lowest viscosity sensitivity and is less sensitive to viscosity change compared to the asymmetric DCM-OH-2-MT, which is probably due to its higher energy barrier for the twisted-intramolecular charge transfer (TICT) process. DCM-OH-2 and DCM-OH-2-DT were then employed to monitor the aggregation of A $\beta_{42}$  peptide since they exhibit lower  $x$  values. In this experiment,



**Figure 4.** a) Viscosity sensitivity measurement of compound DCM-OH-2, DCM-OH-2-MT and DCM-OH-2-DT in ethylene glycol and glycerol mixture. Liner fitting based on equation:  $\log(I) = x \log(\eta) + C$ . b) Summarized Viscosity sensitivity values obtained from the slope ( $x$ ) of the liner fitting. c) Detection of A $\beta_{42}$  aggregation by ThT, DCM-OH-2, and DCM-OH-2-DT. \* From Ref. [21].

ThT showed minimal fluorescence enhancement from 0–10 h, mainly because ThT cannot detect the less aggregated  $A\beta_{42}$  oligomers that are formed initially. In contrast, DCM-OH-2 and DCM-OH-2-DT showed more significant fluorescence increases at the early stage of the aggregation process (Figure 4c). Further fluorescence enhancement was observed until 40 h when the mature  $A\beta$  fibrils are formed.

After demonstrating the *in vitro* interactions between the DCM-based RBFs with  $A\beta$  aggregates, we then investigated their interactions with native  $A\beta$  aggregates in 5xFAD mouse brain sections. 5xFAD mouse is commonly used as an AD mouse model that generates various  $A\beta$  aggregates in the brain.<sup>[27]</sup> Individual brain slices with 40  $\mu\text{m}$  thickness sectioned from 9-month-old AD brains were employed during these experiments. ThS, which is widely used to label *ex vivo*  $A\beta$  aggregates on mouse brain sections, was applied in the colocalization experiments (Figure 5a).<sup>[28]</sup> Compound DCM-OH-2 demonstrates a comparable labeling pattern to ThS and exhibits binding to the identical core regions of the  $A\beta$  aggregates, which represent the more condensed and heavily aggregated fibrillar species.<sup>[29]</sup> Interestingly, compounds DCM-OH-2-MT and DCM-OH-2-DT bind to the peripheral region of the  $A\beta$  aggregates and surround the fluorescent signals from ThS. The peripheral regions of  $A\beta$  aggregates on the brain sections were shown to be less aggregated oligomeric  $A\beta$  species.<sup>[10a]</sup> From these labeling results, compared to ThS and DCM-OH-2, the amphiphilic compounds DCM-OH-2-MT and

DCM-OH-2-DT were shown to interact with the oligomeric  $A\beta$  species.

To serve as imaging agents for *in vivo* studies, these compounds should also be able to cross the blood–BBB readily. Thus, the lipophilicity of the compounds was measured via partition coefficient measurements, to reveal LogD values between 0.9 to 1.7 (Table S3), indicating their potential to cross BBB.<sup>[30]</sup> Indeed, when 12-month-old 5xFAD mice were treated with DCM-OH-2-DT for 10 days at 1 mg/kg, we have observed the brain accumulation of the compound bound to  $A\beta$  aggregates, which is further confirmed by the post-colocalization experiments with ThS (Figure 5b). Overall, these results strongly suggest that the compound can successfully cross the BBB and bind to the native  $A\beta$  species.

### Real-time *in vivo* imaging with amphiphilic compounds

Given the promising *in vitro* results, we were motivated to explore the *in vivo* imaging capabilities of the developed compounds. The cytotoxicity of the DCM compounds towards both mouse neuroblastoma (N2A) and human neuroblastoma (SH-SY5Y) cells was first evaluated. In general, DCM derivatives behave similarly and induced no obvious cytotoxicity to both cells (Figures S10 and S11). DCM-OH-2 is slightly more toxic than the others, possibly due to its poor solubility in the cell media. This also emphasizes the importance of the hydrophilic TACN groups, which help to increase the solubility of the

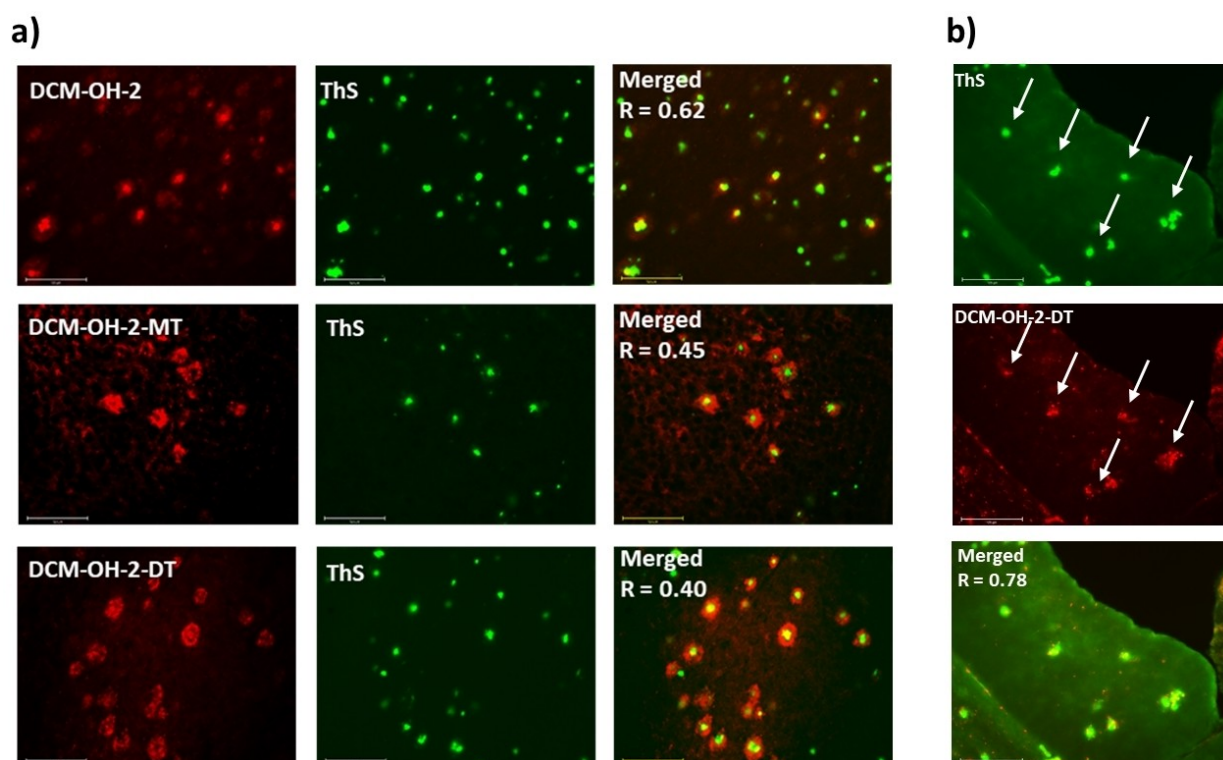


**Figure 5.** a) Fluorescence microscopy images of 9-month-old 5xFAD mice brain sections co-incubated with the DCM-based compounds (left), ThS (middle) and merged images (right, along with the Pearson's correlation coefficients R). Concentrations: [compound] = 10  $\mu\text{M}$ , [ThS] = 2.5  $\mu\text{M}$ ; scale bar: 125  $\mu\text{m}$ . b) Brain sections were collected from 12-month-old AD mice treated with the DCM-OH-2-DT for 10 days at 1 mg/kg. Fluorescence microscopy images of the brain sections stained with ThS. Conditions: [ThS] = 5  $\mu\text{M}$ , scale bar: 125  $\mu\text{m}$ .

compounds, and thus improve their *in cellulo* and *in vivo* performance. Based on all the above studies, DCM-OH-2-DT was chosen as the best candidate for the real-time *in vivo* fluorescence imaging studies. Seven-month-old AD mice and age-matched wild type (WT) mice were injected with the compound at 5 mg/kg. The NIR fluorescence intensities from the brain region were collected and analyzed over time. The signal from DCM-OH-2-DT increased to the maximum about 15 min after the injection, followed by a slow clearance of the compound. When comparing the signal intensity with WT mice, excitingly, DCM-OH-2-DT exhibited significantly higher fluorescence signal in AD mice at 5-, 15-, and 30-min post injection (Figures 6a and 6b). These imaging results further support the potential *in vivo* application of the developed compounds. Additionally, DCM-OH-2-DT is able to differentiate the AD mice vs. WT at a relative early age (7 months old), suggesting its potential application as an early diagnostic agent for AD.

### Copper chelating abilities of the amphiphilic compounds

The triazamacrocyclic TACN group serves as a common ligand framework to chelate Cu and is widely used in  $^{64}\text{Cu}$ -based PET imaging applications. Our group has demonstrated that phenol with  $\text{Me}_2\text{TACN}$  or other TACN derivatives are able to chelate  $^{64}\text{Cu}$  efficiently and strongly.<sup>[31]</sup> However, the Cu-chelating abilities of a phenol moiety with two TACN groups attached have never been investigated. Job's plot analysis was first

performed to analyze the stoichiometry of the Cu(II)-ligand complexation in solution. For DCM-OH-1-MT and DCM-OH-1-DT, the breaks in the plots occur in between 0.33 and 0.5 Cu mole fraction, indicating a mixture of 1:1 and 2:1 ligand-to-Cu complexes in solution, while for DCM-OH-2-DT only the 1:1 ligand-to-Cu complexes were observed (Figure S12). We postulate that the electron donating ability of the phenol groups affected by the numbers of double bonds can lead to the stoichiometry difference of the Cu(II)-ligand complexes formed in solution. Furthermore, spectrophotometric titrations were performed on the Cu(II) complexes to determine the corresponding stability constants (Figure S13 and S14). Interestingly, DCM compounds with one double bond showed higher affinities (Log K) towards Cu, about ~1 or 2 orders of magnitude larger than that of DCM compounds with two double bonds (Table 1). Moreover, DCM-based compounds with two TACN groups attached also showed higher stability constants than the MT-based compounds, which is probably due to the extra chelating abilities of the TACN group (Table 1). Finally, the concentrations of free Cu(II) ( $\text{pM} = -\log[M_{\text{unchelated}}]$ ) at a specific pH value can be calculated from the speciation plots. The calculated pCu values with 1:1 ligand to Cu ratio for the DCM compounds at pH 6.6 and pH 7.4 are comparable to the strong Cu chelating agent DTPA (Table S4).<sup>[32]</sup> Overall, these results show that the amphiphilic DCM compounds can chelate Cu strongly and have the potential to be used as  $^{64}\text{Cu}$  chelating agents for PET imaging of AD, which is a focus of our current research efforts.

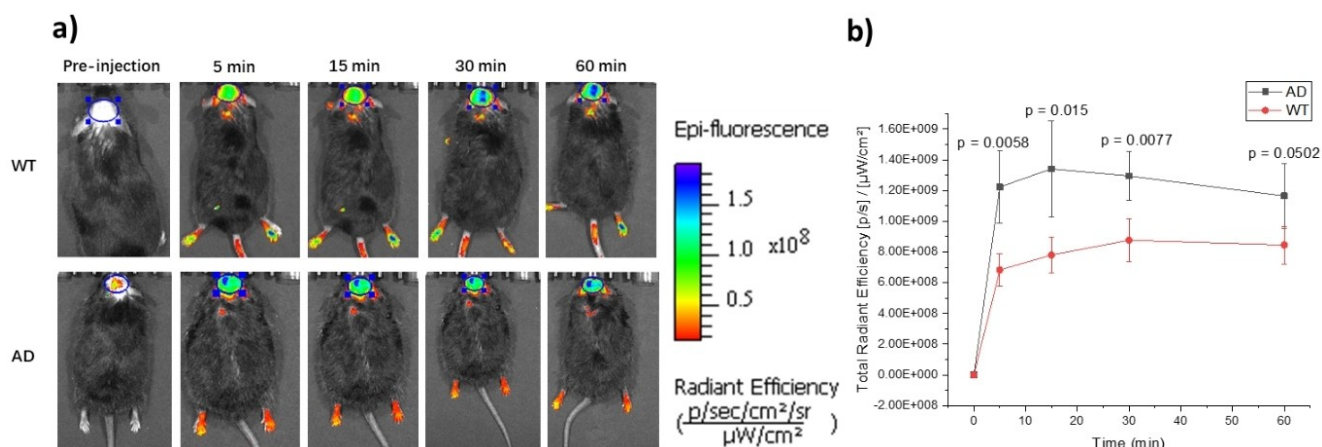


**Figure 6.** a) Representative images of 5x9AD mice and control mice at different time points before and after injection of the compound DCM-OH-2-DT (5 mg/kg). Excitation filter 465 nm, emission filter 740 nm b) Quantitative analysis of fluorescence signals in the brain region from transgenic 5x9AD mice and control mice (n = 3) at preinjection and 5, 15, 30, 60 min after injection. The signals were significantly higher in 7-month-old 5x9AD mice than in the age-matched control mice. P values were calculated by Student's t test.

Table 1. Summarized stability constants (Log K) for the ligand-Cu(II) complexes.				
	DCM-OH-1-MT	DCM-OH-1-DT	DCM-OH-2-MT	DCM-OH-2-DT
$\text{M}^{2+} + \text{HL}^+ = [\text{MHL}]^{3+}$	4.86(2)	6.39(7)	5.32(3)	5.29(5)
$\text{M}^{2+} + \text{L} = [\text{ML}]^{2+}$	14.13(1)	16.57(3)	13.14(2)	13.62(3)
$[\text{ML}(\text{H}_2\text{O})]^{2+} = [\text{ML}(\text{OH})]^+ + \text{H}^+$			4.62(3)	6.72(3)

## Conclusions

In summary, we have developed a new zwitterionic ES IPT system enabled by triazacyclononane (TACN) groups attached to the DCM scaffold. Interestingly, when two TACN groups are attached, the zwitterionic ES IPT process is extremely efficient and emits in the NIR region in physiologically relevant aqueous media. The imaging applications of the developed compounds were further investigated in the context of AD. We successfully demonstrated that compound DCM-OH-2-DT binds to A $\beta$  oligomers in vitro and to the native A $\beta$  aggregates in vivo. We also showed that DCM-OH-2-DT is a strong chelator for Cu and has the potential to be labeled with <sup>64</sup>Cu, to serve as a potential <sup>64</sup>Cu PET imaging agent for AD. Overall, we believe the dual-imaging capabilities of these compound will benefit both preclinical and clinical studies for AD. The photophysical properties of these molecules could be further tuned by substituting the electron acceptor (dicyanomethylene) or the electron donor (phenol group) with other strong electron withdrawing groups or hydrogen bond donors (such as aniline with a labile N–H proton).<sup>[33]</sup> In addition, to expand the functionality of these molecules, the phenol group could be readily capped with a variety of triggers that could be reactive only in presence of specific analytes, to generate various reactivity-based imaging agents.<sup>[34]</sup> Thus, our studies provide a general molecular design strategy for developing new zwitterionic ES IPT compounds with NIR emission for further in vivo imaging applications.

## Experimental Section

**General Information.** All reagents and solvents were purchased from commercial sources and used without further purification unless otherwise stated. 1,4-Dimethyl-1,4,7-triazacyclononane (Me<sub>2</sub>HTACN) was synthesized according to reported procedures.<sup>[35]</sup> HRMS data were obtained on a high-resolution electrospray ionization mass spectrometry (HR-ESI-MS, Thermo Scientific™ LTQ Orbitrap XL™ Hybrid Ion Trap-Orbitrap) (Thermo Scientific, USA). UV-visible spectra were recorded on a Varian Cary 50 Bio spectrophotometer, and fluorescence emission spectra were measured by a SpectraMax M2e plate reader (Molecular Devices, USA). Fluorescence images for brain sections were visualized using an Invitrogen EVOS FL Auto 2 Imaging System (Thermo Fisher, USA). Colocalization analysis and determination of the Pearson's correlation coefficient was performed with the imaging software Fiji. The mouse neuroblastoma N2A and human neuroblastoma SH-SY5Y cell lines were purchased from Millipore Sigma (USA). Compound purification was performed on a Teledyne Isco Combiflash Rf+. <sup>1</sup>H and <sup>13</sup>C NMR spectra were recorded on Varian 500 or Bruker B500 spectrometers. Spectra were analyzed and visualized with MestReNova (15.0). All other data analysis was performed using GraphPad Prism (8.0) or Origin 2020. 5xFAD transgenic mice overexpressing mutant human APP (695) with the Swedish (K670N, M671L), Florida (I716V), and London (V717I) were purchased from Jackson Laboratories (USA).

**Absorbance spectra, fluorescence excitation and emission spectra.** Absorbance spectra were collected using an Agilent Cary 50 Bio spectrophotometer and were normalized against its maxima to give the finalized spectra. Compounds were diluted from 5 mM DMSO stock solution to a final concentration of 10  $\mu$ M with the

corresponding solvents and the emission spectra were collected at room temperature in a quartz cuvette via a plate reader (SpectraMax M2e, Molecular Devices, USA). The corresponding excitation spectra were also obtained in a quartz cuvette via a plate reader. Each spectrum was normalized against its maxima to give the finalized spectra.

**DFT and TD-DFT calculations.** All quantum chemical calculations—density functional theory (DFT) and time-dependent density functional theory (TD-DFT) were performed using the Gaussian 16 electronic structure program.<sup>[36]</sup> Geometry optimizations and frequency calculations were performed on the ground state structures ( $S_0$ ) of DCM-OH-2, DCM-OH-2-MT and DCM-OH-2-DT using the B3LYP hybrid density functional, along with the 6–311G(d) basis set.<sup>[37]</sup> The absorption and emission wavelengths were obtained via TD-DFT vertical excitation energy calculations at the obtained  $S_0$  and  $S_1$  optimized structures, respectively. TD-DFT studies were performed with CAM-B3LYP hybrid density functional, along with the 6-31G(d) basis set. The solvent effect of water was considered using the built-in SMD model.<sup>[38]</sup> Structures were confirmed to be true minima, as vibrational analysis showed no imaginary frequencies. Cartesian coordinates for the optimized geometries in  $S_0$  and  $S_1$  are given in Tables S4. Frontier molecular orbitals analysis and the HOMO→LUMO gap of the compounds in the water are shown in Figure S15.

**Preparation of the A $\beta_{42}$  fibrils and A $\beta_{42}$  oligomers.** Monomeric A $\beta_{42}$  preparation for further incubation: 1 mg of commercial A $\beta_{42}$  monomer powder (from GL biochem) was dissolved with 1 mL 1,1,1,3,3,3-hexafluoro-2-propanol (HFIP) at room temperature and incubated for 1 h. The resulting solution was divided equally into two Eppendorf tubes. Each Eppendorf tube containing 0.5 mg A $\beta_{42}$  monomer was then evaporated overnight under vacuum and dried completely by vacuum centrifuge to generate monomeric films. 100  $\mu$ M A $\beta_{42}$  fibrils solution preparation: the 0.5 mg monomeric films were redissolved in 1.1 mL PBS buffer (with final DMSO concentration less than 1%) and stirring at 37 °C for 3 days with a thermomixer. A $\beta_{42}$  oligomers preparation: the 0.5 mg monomeric films were dissolved in 1.1 mL PBS buffer (with final DMSO concentration less than 1%) and incubated at 4 °C overnight. The resulting solution was then centrifuged at 3000 rpm for 15 min to remove the insoluble aggregates. The clear supernatant was then used for the following experiments. The concentration of the soluble A $\beta_{42}$  oligomers solution was checked by measuring the absorbance of the supernatant at 280 nm and calculated with the molar extinction coefficient of 1480 M<sup>-1</sup> cm<sup>-1</sup>.

**Fluorescence turn-on effects of the compounds with A $\beta_{42}$  fibrils and A $\beta_{42}$  oligomers.** All fluorescence spectra were recorded with a SpectraMax M2e plate reader (Molecular Devices, USA). ThT fluorescence turn-on assays were always performed as a control to check the formation of A $\beta_{42}$  fibrils and oligomers. The fluorescence spectra of ThT in PBS (100  $\mu$ L PBS, 10  $\mu$ M) were recorded as the baseline. Then A $\beta_{42}$  fibrils or oligomers were added to ThT in PBS to make a 100  $\mu$ L mixture and the final concentrations of ThT and A $\beta_{42}$  species were 10  $\mu$ M and 25  $\mu$ M, respectively. To measure the fluorescence turn-on effects of and compounds towards A $\beta$ s, the fluorescence spectra of the compounds' solution (100  $\mu$ L PBS, 5.0  $\mu$ M) were recorded as the baseline without adding A $\beta_{42}$  species. Then A $\beta_{42}$  fibrils or oligomers were added to compounds in PBS to make a 100  $\mu$ L mixture and the final concentrations of the compound and A $\beta_{42}$  species were 5  $\mu$ M and 25  $\mu$ M, respectively.

**In vitro saturation binding studies with A $\beta_{42}$  fibrils and A $\beta_{42}$  oligomers.** Fluorescence saturation assays were performed to determine the binding affinities of the compounds towards different A $\beta_{42}$  aggregates. To a solution of increasing concentrations of compounds in PBS, a fixed concentration of the aggregated A $\beta_{42}$

fibrils or A $\beta_{42}$  oligomers solutions was added to yield a total volume of 100  $\mu$ L. Nonspecific binding was recorded without A $\beta$ s as the baseline. All concentrations were conducted in triplicates. The whole mixture was then incubated for 15 min at room temperature before the measurements. The fluorescent intensity was recorded in a nonbinding 96-well plate with a SpectraMax M2e plate reader (Molecular Devices, USA). The corresponding  $K_d$  curves were generated by GraphPad Prism 8.0 with one site-specific binding model. Equation:  $Y = B_{\max} * X / (K_d + X)$ .

**Selectivity and photostability measurements.** For the selectivity measurements, 5  $\mu$ M DCM-OH-2-MT or 5  $\mu$ M DCM-OH-2-DT were incubated with different analytes in PBS, and the fluorescence intensity of DCM-OH-2-MT and DCM-OH-2-DT were recorded at 620 nm and 730 nm, respectively (excitation wavelength 470 nm). [A $\beta_{42}$  fibrils] = [Cysteine] = [Histidine] = [Arginine] = [Alanine] = [Aspartic acid] = [Sodium ascorbate] = [LiCl] = [KCl] = [CaCl<sub>2</sub>] = [ZnCl<sub>2</sub>] = [FeCl<sub>3</sub>] = [CuCl<sub>2</sub>] = 50  $\mu$ M. [BSA] = [HSA] = 1 mg/mL. For the photostability measurements, the fluorescence intensity of 5  $\mu$ M DCM-OH-2-MT or 5  $\mu$ M DCM-OH-2-DT in the presence or absence of 50  $\mu$ M A $\beta_{42}$  fibrils in PBS were recorded every 20s over a duration of one hour, at 620 nm and 730 nm, respectively (excitation wavelength 470 nm).

**Molecular docking studies.** Molecular docking studies on amphiphilic molecules with A $\beta_{42}$  tetramers (PDB ID: 6RHY) and A $\beta_{42}$  fibrils (PDB ID: 5OQV) were performed using Schrödinger Suite software. Ligprep program was used to prepare ligand structures at pH 7.0  $\pm$  2.0. Protein Preparation Wizard program was used to optimize protein structures with the OPLS3 force field. The grid size was adjusted to encompass the entire optimized protein structure in every direction. Glide program was used for the final molecular docking, with the poses ranked based on both the docking score and Glide e-model energy. The structures with the best docking scores and Glide e-model energies were subsequently visualized using PyMol.

**Cytotoxicity studies.** Alamar Blue assay was chosen for the cytotoxicity studies. Then N2A cells or SH-SY5Y cells were seeded in a 96-well plate ( $2.0 \times 10^4$ /well). After 24 h incubation, cell media was changed to DMEM/N-2 for N2A or MEM/F-12 (1:1)/N-2 for SH-SY5Y, and then cells were incubated for another 1 h. After treating the cells with different concentrations of compounds for 40 h, Alamar Blue solution (10  $\mu$ L) was added, and the mixture were incubated for another 90 min at 37 °C. The fluorescence intensity of each well was measured at 590 nm (excitation wavelength = 560 nm).

**Histological staining of 5xFAD mice brain sections.** For the colocalization experiments between the compounds and ThS: 9-month-old 5xFAD transgenic mice brain sections were blocked with bovine serum albumin (2% BSA in PBS, pH 7.4, 10 min). Then the mice brain sections were stained with 10  $\mu$ M compound in PBS for 1 h and were sequentially incubated with 2.5  $\mu$ M ThS in PBS for another 1 h. Then the brain sections were treated with BSA again (5 min) followed by washing with PBS (3 $\times$ 2 min), DI water (3 $\times$ 2 min). Finally, non-fluorescent mounting medium was used to mount the mouse brain sections, and EVOS FL Auto 2 was used to capture the images. ImageJ Fiji program was used for colocalization analysis and determination of the Pearson's correlation coefficient. To confirm the BBB permeability for DCM-OH-2-DT and the in vivo A $\beta$  binding ability, the brain sections from DCM-OH-2-DT treated 5xFAD mice were directly stained with 5  $\mu$ M ThS, followed by the same incubation and wash steps for in vitro brain sections staining. The images were obtained by using EVOS FL Auto 2. ImageJ Fiji program was used for colocalization analysis and determination of the Pearson's correlation coefficient.

**Log D measurements.** The Log D measurements was performed by following a published procedure.<sup>[39]</sup> In general, compounds in 0.5 mL octanol were subjected to partition with 0.5 mL octanol-saturated PBS. The whole mixture was stirred vigorously for 5 min, and centrifuged at 2,000 rpm for 5 min. The top octanol layer was separated for later fluorescence measurement. The remaining PBS layer was partitioned with 0.5 mL PBS-saturated octanol, and the second top octanol layer was then separated after vigorous stirring and centrifuging at 2,000 rpm for another 5 min. The two octanol layers' fluorescence spectra were recorded. The log D value was calculated by the fluorescence intensity ratio at the compounds' emission wavelength for the above two octanol extractions.

**Viscosity sensitivity measurements.** Viscosity sensitivity was measured according to previous published procedures.<sup>[11b]</sup> 10  $\mu$ M compounds (DCM-OH-2, DCM-OH-2-MT and DCM-OH-2-DT) were diluted from 5 mM DMSO stock solution into a series of ethylene glycol (EG) and glycerol (G) mixture: EG/G = 50/50 (183 cP), 40/60 (283 cP), 30/70 (426 cP), 20/80 (621 cP), 0/100 (1069 cp). All samples were thoroughly mixed till no layer separation observed. Then, 100  $\mu$ L of each sample was transferred to a 96-well plate for recording the fluorescence intensity. Based on the Förster-Hoffmann equation  $\log I = x \log \eta + A$ , a logarithm plot of emission intensity as a function of viscosity was fitted by linear regression.  $\eta$  is viscosity (cP),  $I$  is the fluorescence intensity,  $x$  is the slope of the regression line that represents the viscosity sensitivity.

**In vitro protein aggregation assay.** To monitor the in vitro aggregation of A $\beta_{42}$  peptide, a solution of 100  $\mu$ M A $\beta_{42}$  monomers in PBS was prepared as described above. The solution was incubated at 37 °C with ThermoMixer for 40 h. Fluorescence intensities were recorded at selected time points by mixing 25  $\mu$ M peptide and 5  $\mu$ M DCM-OH-2, DCM-OH-2-DT or ThT in PBS at their corresponding excitation. The emission was recorded at 620 nm for DCM-OH-2, 740 nm for DCM-OH-2-DT, and 485 nm for ThT. Fluorescence intensity was normalized against the maxima from each compound to give the finalized graph.

**Job's plot analysis.** A series of solutions in PBS (pH 7.4) with fixed total concentration of 30  $\mu$ M (compound + Cu), which contain different ratios of compound and Cu (II) from 0 to 100 mol % Cu, were prepared. The mixture was allowed to equilibrate for at least 5 min at room temperature and the corresponding UV-vis spectra were collected.

**pKa and stability constant measurements.** UV-vis spectrophotometric titrations were performed to determine the acidity constants (pKa) of the developed compounds and stability constants for their Cu(II) complexes. In general, solutions of ligands (about 20  $\mu$ M, 0.1 M NaCl) or ligands + Cu(II) (30  $\mu$ M, 0.1 M NaCl) were titrated with small aliquots of 0.2 M NaOH at room temperature under a steady moist flow of N<sub>2</sub>, from low pH to high pH at room temperature until no more spectral changes observed (pH range 3–11). About 30 spectra were collected for each compound or complex, the corresponding acidity and stability constants were then calculated using the HypSpec computer program (Protonic Software, UK).<sup>[40]</sup> Speciation plots of the compounds and their metal complexes were calculated using the program HySS2009 (Protonic Software, UK).<sup>[41]</sup>

**Animal studies.** Experiments involving animals were performed in compliance with the Institutional Animal Care and Use committee of the University of Illinois at Urbana-Champaign (IACUC protocol # 22094). For the animal treatment experiments, 12-month-old 5xFAD mice were treated daily with a solution of DCM-OH-2-DT in PBS (1 mg/kg of body weight, pH 7.4) via intraperitoneal injection. After 10 days of treatment, all mice brains were harvested after perfusion. The real-time in vivo fluorescence imaging studies were

performed with IVIS imaging system. 7-month-old 5xFAD mice ( $n = 3$ ) and age-matched control B6SJL/F1/J mice ( $n = 3$ ) were shaved at the brain region before background imaging. All mice were injected with DCM-OH-2-DT (5 mg/kg, 15% DMSO, 85% PBS) via jugular vein injection. The mice were kept on the imaging stage under anesthesia with 2.5% isoflurane gas in an oxygen flow (1.5 L/min) before the imaging and were woken up after the imaging. Fluorescence signals from the brain were recorded at 5-, 15-, 30-, 60-min after the injection of DCM-OH-2-DT with a filter set (excitation at 470 nm and emission at 740 nm). Imaging data was analyzed by Living Image software, and an ROI was drawn around the brain region. The data were analyzed by subtracting the background fluorescence intensity of each mouse. P values were calculated by Student's *t* test.

## Supporting Information

Additional experimental and synthetic details. The authors have cited additional references within the Supporting Information.<sup>[11b,35–42]</sup>

## Acknowledgements

This work was supported by research funding from the NIH (R01GM114588 to L.M.M.).

## Conflict of Interests

A provisional patent (U.S. Patent Application No. 63/389,270, Title: "Amphiphilic Compounds for attenuating neurotoxicity of amyloid-beta oligomers and diagnostic methods", Inventors: Liviu M. Mirica and Zhengxin Yu, Filing date: July 14, 2022) has been filed on the synthesis and applications of the compounds described herein. All authors declare no other competing interests.

## Data Availability Statement

The data that support the findings of this study are available in the supplementary material of this article.

**Keywords:** Alzheimer's disease · amyloid- $\beta$  oligomers · early diagnosis · near-infrared fluorescence imaging · zwitterionic excited-state intramolecular proton transfer

- [1] A. Weller, *Naturwissenschaften* **1955**, *42*, 175–176.
- [2] a) A. C. Sedgwick, L. Wu, H.-H. Han, S. D. Bull, X.-P. He, T. D. James, J. L. Sessler, B. Z. Tang, H. Tian, J. Yoon, *Chem. Soc. Rev.* **2018**, *47*, 8842–8880; b) V. S. Padalkar, S. Seki, *Chem. Soc. Rev.* **2016**, *45*, 169–202.
- [3] a) M. M. Henary, Y. Wu, C. J. Fahrni, *Chem. Eur. J.* **2004**, *10*, 3015–3025; b) S. Barman, S. K. Mukhopadhyay, M. Gangopadhyay, S. Biswas, S. Dey, N. D. P. Singh, *J. Mater. Chem. B* **2015**, *3*, 3490–3497.
- [4] a) N. Suzuki, A. Fukazawa, K. Nagura, S. Saito, H. Kitoh-Nishioka, D. Yokogawa, S. Irle, S. Yamaguchi, *Angew. Chem. Int. Ed.* **2014**, *53*, 8231–8235; b) C.-H. Wang, Z.-Y. Liu, C.-H. Huang, C.-T. Chen, F.-Y. Meng, Y.-C. Liao, Y.-H. Liu, C.-C. Chang, E. Y. Li, P.-T. Chou, *J. Am. Chem. Soc.* **2021**, *143*, 12715–12724; c) A. Shukla, V. T. N. Mai, V. V. Divya, C. H. Suresh, M.

- Paul, V. Karunakaran, S. K. M. McGregor, I. Allison, K. N. Narayanan Unni, A. Ajayaghosh, E. B. Namdas, S.-C. Lo, *J. Am. Chem. Soc.* **2022**, *144*, 13499–13510; d) T. Mutai, H. Tomoda, T. Ohkawa, Y. Yabe, K. Araki, *Angew. Chem. Int. Ed.* **2008**, *47*, 9522–9524.
- [5] a) J. Hardy, D. J. Selkoe, *Science* **2002**, *297*, 353–356; b) M. G. Spillantini, M. L. Schmidt, V. M. Y. Lee, J. Q. Trojanowski, R. Jakes, M. Goedert, *Nature* **1997**, *388*, 839–840.
- [6] a) E. Karran, M. Mercken, B. De Strooper, *Nat. Rev. Drug Discovery* **2011**, *10*, 698–712; b) V. W. Chow, M. P. Mattson, P. C. Wong, M. Gleichmann, *NeuroMol. Med.* **2010**, *12*, 1–12.
- [7] a) I. Benilova, E. Karran, B. De Strooper, *Nat. Neurosci.* **2012**, *15*, 349–357; b) S. J. C. Lee, E. Nam, H. J. Lee, M. G. Savelieff, M. H. Lim, *Chem. Soc. Rev.* **2017**, *46*, 310–323; c) E. N. Cline, M. A. Bicca, K. L. Viola, W. L. Klein, *J. Alzheimer's Dis.* **2018**, *64*, S567–S610.
- [8] a) P. H. Nguyen, A. Ramamoorthy, B. R. Sahoo, J. Zheng, P. Faller, J. E. Straub, L. Dominguez, J.-E. Shea, N. V. Dokholyan, A. De Simone, B. Ma, R. Nussinov, S. Najafi, S. T. Ngo, A. Loquet, M. Chiricotto, P. Ganguly, J. McCarty, M. S. Li, C. Hall, Y. Wang, Y. Miller, S. Melchionna, B. Habenstein, S. Timr, J. Chen, B. Hnath, B. Strodel, R. Kayed, S. Lesné, G. Wei, F. Sterpone, A. J. Doig, P. Derreumaux, *Chem. Rev.* **2021**, *121*, 2545–2647; b) S. Ciudad, E. Puig, T. Botzanowski, M. Meigooni, A. S. Arango, J. Do, M. Mayzel, M. Bayoumi, S. Chaignepain, G. Maglia, S. Cianferoni, V. Orekhov, E. Tajkhorshid, B. Bardiaux, N. Carulla, *Nat. Commun.* **2020**, *11*, 3014.
- [9] A. Aliyan, N. P. Cook, A. A. Martí, *Chem. Rev.* **2019**, *119*, 11819–11856.
- [10] a) C. L. Teoh, D. Su, S. Sahu, S. W. Yun, E. Drummond, F. Prelli, S. Lim, S. Cho, S. Ham, T. Wisniewski, Y. T. Chang, *J. Am. Chem. Soc.* **2015**, *137*, 13503–13509; b) Y. Li, D. Xu, A. Sun, S. L. Ho, C. Y. Poon, H. N. Chan, O. T. W. Ng, K. K. L. Yung, H. Yan, H. W. Li, M. S. Wong, *Chem. Sci.* **2017**, *8*, 8279–8284; c) G. Lv, A. Sun, P. Wei, N. Zhang, H. Lan, T. Yi, *Chem. Commun.* **2016**, *52*, 8865–8868; d) Y. Li, J. Yang, H. Liu, J. Yang, L. Du, H. Feng, Y. Tian, J. Cao, C. Ran, *Chem. Sci.* **2017**, *8*, 7710–7717; e) G. L. Lv, A. Y. Sun, M. Q. Wang, P. Wei, R. H. Li, T. Yi, *Chem. Commun.* **2020**, *56*, 1625–1628; f) J. Yang, F. Zeng, X. Li, C. Ran, Y. Xu, Y. Li, *Chem. Commun.* **2020**, *56*, 583–586.
- [11] a) Y. Liu, C. H. Wolstenholme, G. C. Carter, H. Liu, H. Hu, L. S. Grainger, K. Miao, M. Fares, C. A. Hoelzel, H. P. Yennawar, G. Ning, M. Du, L. Bai, X. Li, X. Zhang, *J. Am. Chem. Soc.* **2018**, *140*, 7381–7384; b) C. H. Wolstenholme, H. Hu, S. Ye, B. E. Funk, D. Jain, C.-H. Hsiung, G. Ning, Y. Liu, X. Li, X. Zhang, *J. Am. Chem. Soc.* **2020**, *142*, 17515–17523.
- [12] B. Alies, H. Eury, E. M. Essassi, G. Pratiel, C. Hureau, P. Faller, *Anal. Chem.* **2014**, *86*, 11877–11882.
- [13] B. Jiang, A. Aliyan, N. P. Cook, A. Augustine, G. Bhak, R. Maldonado, A. D. Smith McWilliams, E. M. Flores, N. Mendez, M. Shahnawaz, F. J. Godoy, J. Montenegro, I. Moreno-Gonzalez, A. A. Martí, *J. Am. Chem. Soc.* **2019**, *141*, 15605–15610.
- [14] a) L. Sun, H.-J. Cho, S. Sen, A. S. Arango, N. Bandara, Y. Huang, T. T. Huynh, B. E. Rogers, E. Tajkhorshid, L. M. Mirica, *J. Am. Chem. Soc.* **2021**, *143*, 10462–10476; b) Z. Yu, W. Guo, S. Patel, H.-J. Cho, L. Sun, L. M. Mirica, *Chem. Sci.* **2022**, *10*, 1039/D1032SC02654F.
- [15] a) H. Rai, S. Gupta, S. Kumar, J. Yang, S. K. Singh, C. Ran, G. Modi, *J. Med. Chem.* **2022**, *65*, 8550–8595; b) H. W. Liu, J. Yang, L. T. Wang, Y. G. Xu, S. Y. Zhang, J. Lv, C. Z. Ran, Y. Y. Li, *Future Med. Chem.* **2017**, *9*, 179–198.
- [16] N. Suzuki, M. Wakioka, F. Ozawa, S. Yamaguchi, *Asian J. Org. Chem.* **2020**, *9*, 1326–1332.
- [17] LiviuNote2020.
- [18] A. P. Demchenko, K.-C. Tang, P.-T. Chou, *Chem. Soc. Rev.* **2013**, *42*, 1379–1408.
- [19] X. Wu, X. Sun, Z. Guo, J. Tang, Y. Shen, T. D. James, H. Tian, W. Zhu, *J. Am. Chem. Soc.* **2014**, *136*, 3579–3588.
- [20] T. Storr, M. Merkel, G. X. Song-Zhao, L. E. Scott, D. E. Green, M. L. Bowen, K. H. Thompson, B. O. Patrick, H. J. Schugar, C. Orvig, *J. Am. Chem. Soc.* **2007**, *129*, 7453–7463.
- [21] S. Ye, H. Zhang, J. Fei, C. H. Wolstenholme, X. Zhang, *Angew. Chem. Int. Ed.* **2021**, *60*, 1339–1346.
- [22] a) W. Fu, C. Yan, Z. Guo, J. Zhang, H. Zhang, H. Tian, W.-H. Zhu, *J. Am. Chem. Soc.* **2019**, *141*, 3171–3177; b) Y. Cheng, B. Zhu, Y. Deng, Z. Zhang, *Anal. Chem.* **2015**, *87*, 4781–4787; c) Y. Cheng, B.-y. Zhu, X. Li, G.-b. Li, S.-y. Yang, Z.-r. Zhang, *Bioorg. Med. Chem. Lett.* **2015**, *25*, 4472–4476.
- [23] W. L. Klein, G. A. Krafft, C. E. Finch, *Trends Neurosci.* **2001**, *24*, 219–224.
- [24] D. Su, W. Diao, J. Li, L. Pan, X. Zhang, X. Wu, W. Mao, *ACS Chem. Neurosci.* **2022**, *13*, 540–551.
- [25] T. Förster, G. Hoffmann, *Z. Phys. Chem.* **1971**, *75*, 63–76.

- [26] a) V. I. Stsiapura, A. A. Maskevich, V. A. Kuzmitsky, V. N. Uversky, I. M. Kuznetsova, K. K. Turoverov, *J. Phys. Chem. B* **2008**, *112*, 15893–15902; b) M. Biancalana, S. Koide, *Biochim. Biophys. Acta* **2010**, *1804*, 1405–1412.
- [27] H. Oakley, S. L. Cole, S. Logan, E. Maus, P. Shao, J. Craft, A. Guillozet-Bongaarts, M. Ohno, J. Disterhoft, L. Van Eldik, R. Berry, R. Vassar, *J. Neurosci.* **2006**, *26*, 10129–10140.
- [28] T. M. Wengenack, S. Whelan, G. L. Curran, K. E. Duff, J. F. Poduslo, *Neuroscience* **2000**, *101*, 939–944.
- [29] D. M. Wilcock, M. N. Gordon, D. Morgan, *Nat. Protoc.* **2006**, *1*, 1591–1595.
- [30] T. T. Wager, R. Y. Chandrasekaran, X. Hou, M. D. Troutman, P. R. Verhoest, A. Villalobos, Y. Will, *ACS Chem. Neurosci.* **2010**, *1*, 420–434.
- [31] a) Y. Wang, T. T. Huynh, N. Bandara, H.-J. Cho, B. E. Rogers, L. M. Mirica, *Dalton Trans.* **2022**, *51*, 1216–1224; b) Y. Wang, T. T. Huynh, H.-J. Cho, Y.-C. Wang, B. E. Rogers, L. M. Mirica, *Inorg. Chem.* **2021**, *60*, 12610–12620.
- [32] A. E. Martell, R. M. Smith, *Critical Stability Constants, Vol. IV*, Plenum, New York, **1976**.
- [33] D. Shen, W. Jin, Y. Bai, Y. Huang, H. Lyu, L. Zeng, M. Wang, Y. Tang, W. Wan, X. Dong, Z. Gao, H.-L. Piao, X. Liu, Y. Liu, *Angew. Chem. Int. Ed.* **2021**, *60*, 16067–16076.
- [34] a) S. H. Gardner, C. J. Brady, C. Keeton, A. K. Yadav, S. C. Mallojjala, M. Y. Lucero, S. Su, Z. Yu, J. S. Hirschi, L. M. Mirica, J. Chan, *Angew. Chem. Int. Ed.* **2021**, *60*, 18860–18866; b) J. Huang, Y. Jiang, J. Li, J. Huang, K. Pu, *Angew. Chem. Int. Ed.* **2021**, *60*, 3999–4003.
- [35] A. K. Sharma, J. W. Schultz, J. T. Prior, N. P. Rath, L. M. Mirica, *Inorg. Chem.* **2017**, *56*, 13801–13814.
- [36] M. J. T. Frisch, G. W.; Schlegel, H. B.; Scuseria, G. E.; Robb, M. A.; Cheeseman, J. R.; Scalmani, G.; Barone, V.; Petersson, G. A.; Nakatsuji, H.; Li, X.; Caricato, M.; Marenich, A. V.; Bloino, J.; Janesko, B. G.; Gomperts, R.; Mennucci, B.; Hratchian, H. P.; Ortiz, J. V.; Izmaylov, A. F.; Sonnenberg, J. L.; Williams-Young, D.; Ding, F.; Lipparini, F.; Egidi, F.; Goings, J.; Peng, B.; Petrone, A.; Henderson, T.; Ranasinghe, D.; Zakrzewski, V. G.; Gao, J.; Rega, N.; Zheng, G.; Liang, W.; Hada, M.; Ehara, M.; Toyota, K.; Fukuda, R.; Hasegawa, J.; Ishida, M.; Nakajima, T.; Honda, Y.; Kitao, O.; Nakai, H.; Vreven, T.; Throssell, K.; Montgomery, J. A., Jr.; Peralta, J. E.; Ogliaro, F.; Bearpark, M. J.; Heyd, J. J.; Brothers, E. N.; Kudin, K. N.; Staroverov, V. N.; Keith, T. A.; Kobayashi, R.; Normand, J.; Raghavachari, K.; Rendell, A. P.; Burant, J. C.; Iyengar, S. S.; Tomasi, J.; Cossi, M.; Millam, J. M.; Klene, M.; Adamo, C.; Cammi, R.; Ochterski, J. W.; Martin, R. L.; Morokuma, K.; Farkas, O.; Foresman, J. B.; Fox, D. J., *Gaussian, Inc., Wallingford CT* **2016**.
- [37] a) A. D. Becke, *J. Chem. Phys.* **1993**, *98*, 5648–5652; b) C. T. Lee, W. T. Yang, R. G. Parr, *Phys. Rev. B: Condens. Matter Mater. Phys.* **1988**, *37*, 785–789.
- [38] A. V. Marenich, C. J. Cramer, D. G. Truhlar, *J. Phys. Chem. B* **2009**, *113*, 6378–6396.
- [39] C. Z. Ran, X. Y. Xu, S. B. Raymond, B. J. Ferrara, K. Neal, B. J. Bacskai, Z. Medarova, A. Moore, *J. Am. Chem. Soc.* **2009**, *131*, 15257–15261.
- [40] P. Gans, A. Sabatini, A. Vacca, *Ann. Chim.* **1999**, *45*.
- [41] L. Alderighi, P. Gans, A. Ienco, D. Peters, A. Sabatini, A. Vacca, *Coord. Chem. Rev.* **1999**, *184*, 311–318.
- [42] a) X. Zeng, Z. Chen, L. Tang, H. Yang, N. Liu, H. Zhou, Y. Li, J. Wu, Z. Deng, Y. Yu, H. Deng, X. Hong, Y. Xiao, *Chem. Commun.* **2019**, *55*, 2541–2544; b) K. Gu, Y. Xu, H. Li, Z. Guo, S. Zhu, S. Shi, T. D. James, H. Tian, W.-H. Zhu, *J. Am. Chem. Soc.* **2016**, *138*, 5334–5340.

Manuscript received: July 26, 2023

Accepted manuscript online: August 24, 2023

Version of record online: October 5, 2023